Journal of Research and Applications in Mechanical Engineering
ISSN: 2229-2152 (Print); 2697-424x (Online)
(2022) Vol. 10, No. 1, Paper No. JRAME-22-10-005
DOI: 10.14456/jrame.2022.5

Research Article

THE COMPUTATIONAL MODELLING IN THE PREDICTION OF FLOW PAST A ROTATING SPHERE AT HIGH REYNOLDS NUMBER

S. Ruchayosyothin[1,*]
P. Konglerd[1]
S. Tamna[2]
[1] *School of Science and Technology, Sukhothai Thammathirath Open University, Nonthaburi, Thailand*
[2] *Department of Mechanical Engineering, Faculty of Engineering, Rajamangala University of Technology Isan, Khonkaen Campus, Khonkaen, Thailand*

Received 12 December 2021
Revised 11 February 2022
Accepted 14 February 2022

ABSTRACT:
The present study has been purposed to predict the convective flow past a rotating sphere at high Reynolds numbers of 10,000, 70,026 and 96,000. The turbulence effects have been examined using the Reynolds stress model (RSM), and strengthens the model effectiveness on strongly curvature surface flow, which the individual form of fluctuation terms have been provided in the second moment closer relating to each physical reason. The RSM has been also used in combination with the strategies of near-wall turbulence of standard log-law-based obtaining the lower computational resource. The predicted result has been assessed through comparisons with available experimental and the present U-RANS approach. The RSM presents a high accuracy result in 3 dimensional flow according to the unpredictable aerodynamic forces along with time history. The lift (C_L)*, drag* (C_D) *and side force* (C_S) *coefficients have been predicted with a wide range of spin ratios up to 5. The maximum values of* C_L *and* C_D *have been found at 0.37 and 0.64 for a rotating sphere, and those of aerodynamic forces have changed with spin ratios. The rotating sphere leads to suppress the wake strength and size downstream. Significantly, the pressure distribution is an asymmetric structure concerning the magnitude of lift, drag coefficients. This research has confirmed that the RSM has been a highly competent approach to examine the convective flow past a rotating sphere at high Reynolds number.*

Keywords: *The Reynolds stress model, Rotating sphere, Turbulence models, High Reynolds number, Magnus force*

1. INTRODUCTION

A rotating sphere with the convective flow has been well known as the Magnus effect [1]. These phenomena have been acknowledged in the widely used in industrial applications from a low to high rotating body sizes such as circulating fluidized bed, nuclear technology, spherical heavy lifting airship, and compound geometry of aerodynamic wings. Moreover, the Magnus effect has concerned in many ball games to obtain the deviation flight path from the common trajectories of a moving body through space, especially, soccer or golf players who have attempted to produce a spinning ball in challenged games [2].

The flow past a rotating sphere has been studied by many previous researchers using experimental and computational method. The asymmetric flow along with parallel and cross flow directions have been found leading to generate

---

* Corresponding author: S. Ruchayosyothin
E-mail address: sitthichai.ruc@stou.ac.th

propulsion forces including lift, drag and side forces, which slightly change with spin ratios (α: proportional tangential velocity of the sphere wall to inlet flow velocity). There have been many researchers showing an increased interest in the flow characteristic at low to high Reynolds number ranges [3].

Since the levels of Reynolds number have mainly been concerned with curved surface and wake boundary layers, in the sub-critical Reynolds number, the boundary layer on the curved surface has played the characteristic in laminar prior to turbulent boundary layer for the next level of Reynolds number and the wake boundary layer has been fully turbulent. Also, the super-critical Reynolds number, the boundary layer on both regions have been found in fully turbulent flow [4]. Consequently, the interaction between convective flow and curved surface has generated the alternated elongated vortices, which comes from the surface boundary layer creation, it has been widely known as "a von Karman vortex street". Those of them have corresponded to the aerodynamic magnitude. Previous several studies of these, have revealed the temporal pattern of flow; It has been clearly periodic on a cylinder surface [5] as opposed to on a sphere surface, which has been unpredictable pattern due to the stronger 3-dimension flow [6], so these evidence has been beneficial to identify the boundary condition in computational method or select the flow measurement on experimental study.

Much of the literature on a sphere has been presented on a stationary test case. The pressure and viscous forces have distributed rapidly changing along a circumferential angle. These patterns have corresponded to drag coefficient, and group Reynolds number in physical ranges. For a sphere, Achenbach [7] has reported the critical Reynolds number of 300,000 because the drag coefficient suddenly drops from 0.5 to less than 0.1. Moreover, the position of separation boundary have also changed with Reynolds number; the azimuthally angle has increased from 80 ° to 120° at Reynolds numbers between 200,000 and 400,000. There has been relatively evidence in curvature surface of a circular cylinder, the gradient of convective fluxes has been rapidly changed along the tangential surface direction, Wieselsberger [8] has presented a smaller critical Reynolds number of 120,000 where the drag coefficient with Reynolds number has been a similar trend and the wake boundary layer has formed in an unstructured geometry.

The experimental studies of a rotating sphere have presented the flow structure expanding the shed around a rotating body, consequently, lift coefficient has suddenly increased then leveled off 0.5 and drag coefficient has been plateaued value of 0.7 when increasing spin ratios up to 3 at sub-critical Reynolds number of 68,000 as reported by Kray et al. [9]. However, the aerodynamic force with spin ratios has trended to discrepancy pattern with moderate Reynolds number of 8,000 the lift coefficient has monotonically grown up and the drag coefficient has suddenly increased to 0.3 at a spin ratio of 3, then it has been decreased approaching 0 with the spin ratio between 1 and 6 as shown in Li & Gao [10].

The computational study has been purposed in so different numerical models and methods in order to clarify the physical details with less computing cost and high accuracy predicted result. The governing equation of Reynold Averaged Navier-Stokes has competent enough to explain the flow phenomena at the low Reynolds number because the flow has been still laminar. Johnson & Patel [6] has provided the strongly 3-dimensional flow interaction leading to generate the un-structured streamlines, however, the flow in time history has been clearly periodic pattern and, moreover, Dobson et al. [11] has reported the Strouhal numbers being around 0.20-0.35 for spin ratios up to 3 at Reynolds number of 300.

As the surface and wake boundary layers have played an essential role in producing the aerodynamic forces. The earlier separation positions on the sphere surface have corresponded to the wake growing in size behind the rotating sphere relating to the attribution of pressure around sphere which distribution patterns have depended on spin ratio and moderate Reynolds number up to 400 which have been executed by finite element approach [12, 13], also, the immersed boundary method has been employed [14]. In the case of a stationary sphere at high Reynolds number test cases, the DES and LES approach with different sub-grid scales have provided data in good agreement results with the earlier experimental study [15]. It has been particularly, the RANS governing equation has a limit in strongly turbulence region, so the LES approach has been used to investigate the flow at spin ratios up to 1 and Reynolds number of 10,000 as reported by Poon et al. [16].

A considerable amount of literature has been published on a sphere, researchers have not treated a rotation body at high Reynolds number in deep detail. The present study has purposed to examine the aerodynamic behavior using the second-moment closer form namely, the Reynolds stress model. The advantage of this current model is that the individual Reynolds Stresses have been included to sensitize the generating turbulence along the 3-D curved surface; there have been available to reproduce the effect of convection, diffusion, production, and dissipation in an anisotropic manner also, the wall correction needs to be resolved for pressure fluctuation reflecting from the wall, which the Reynolds stress normal to the wall suddenly dropping than other components, so the model has been suitable for convective flow of this case. The finite volume scheme has been implemented to discretize the rapid change fluxes between particular and neighbor volume. As apart of a good modeled physics in the hierarchy of turbulence modelling approach, the solving process in computational complexity theory has regarded to low executing resource.

This research has been to strengthen the earlier experimental work with the honest turbulent approach at a high Reynolds number of 70,026 and 96,000 [2, 9]. Also, the moderated Reynolds number of 10,000 has been required with one-half of the turbulent intensity and higher spin ratio [16]. These of them have provided a piece of good scientific information in the area of turbulence regime and aerodynamic behavior for widely used in aircraft, vessel, and industrial energy systems.

2. TURBULENCE MODELLING

The instantaneous velocity ($\mathrm{U_i}$) comprises the time-averaged velocity ($\overline{\mathrm{U}}_\mathrm{i}$) and the instantaneous fluctuation flux (u'_i). As the unsteady Reynolds averaged Navier-Strokes (U-RANS) approach the governing equations for the time-averaged momentum has been adopted the form:

$$\frac{\partial \overline{U}_i}{\partial t}+\frac{\partial(\overline{U}_i\overline{U}_j)}{\partial x_j}=-\frac{1}{\rho}\frac{\partial P}{\partial x_i}+\frac{\partial}{\partial x_j}\left(\nu\frac{\partial \overline{U}_i}{\partial x_j}-\overline{u'_iu'}_j\right) \tag{1}$$

Where the second moment of the fluctuating velocity, ($\mathrm{u'_iu'_j}$), which includes in equation (1) above, also known as the Reynolds stresses, are distributed within the flow field. The unknown needs to be approximated through the introduction of the turbulence modelling equations, within the effective viscosity approximation the Reynolds stresses are assumed to relative linearly on the mean strain rate through Eqs. (2) and (3):

$$\overline{u_iu_j}=\frac{2}{3}k\delta_{ij}-\nu_t\left(\frac{\partial \overline{U}_i}{\partial x_j}+\frac{\partial \overline{U}_j}{\partial x_i}\right) \tag{2}$$

$$\nu_t=C_\mu f_\mu\frac{k^2}{\varepsilon} \tag{3}$$

Where k and ε, are the turbulent kinetic energy and its dissipation rate which are obtained from each transport equation.

The more elaborate Reynolds stress equation, involves the solution of separate transport equations for an individual component of the Reynolds stress tensor, as shown in Eq. (4) below:

$$\frac{\partial}{\partial t}(\rho\overline{u'_iu'_j})+\frac{\partial}{\partial x_k}(\rho\overline{U}_k\overline{u'_iu'_j})=\frac{\partial}{\partial x_k}d_{ijk}+\rho(P_{ij}+\Phi_{ij}-\varepsilon_{ij}) \tag{4}$$

The generation rate of the turbulence stress by mean strain is

$$P_{ij}=-\left(\overline{u'_iu'_k}\frac{\partial \overline{U}_j}{\partial x_k}+\overline{u'_ju'_k}\frac{\partial \overline{U}_i}{\partial x_k}\right) \tag{5}$$

The pressure-strain correlation is

$$\Phi_{ij} = \Phi_{ij}^{(1)} + \Phi_{ij}^{(2)} + \Phi_{ij}^{(w)} \tag{6}$$

The completed pressure-strain term has been modelled and introduced in major three terms as Eq. (7). The first term on the right hand side indicates anisotropic reduction form due to large turbulence-turbulence interaction (a slowly anisotropic reduction process), ($\Phi_{ij}^{(1)}$). The second term relates to anisotropic reduction form due to small eddies interaction (a rapidly anisotropic reduction process), ($\Phi_{ij}^{(2)}$). Also, the rest of those show the wall reflection term due to the pressure fluctuation around the wall ($\Phi_{ij}^{(W)}$).

$$\begin{aligned}\Phi_{ij} = -c_1\varepsilon a_{ij} - c_2\left(P_{ij} - \frac{1}{3}P_{kk}\delta_{ij}\right) + c_{1w}\frac{\varepsilon}{k}\left(\overline{u'_l u'_m} n_l n_m \delta_{ij} - \frac{3}{2}\overline{u'_i u'}_m n_j n_l - \frac{3}{2}\overline{u'_j u'}_l n_i n_l\right)\left(\frac{\iota}{2.5y}\right) \\ + c_{2w}\frac{\varepsilon}{k}\left(\phi_{lm2} n_l n_m \delta_{ij} - \frac{3}{2}\phi_{li2} n_l n_j - \frac{3}{2}\phi_{lj2} n_l n_i\right)\left(\frac{\iota}{2.5y}\right)\end{aligned} \tag{7}$$

where Reynolds stress anisotropic tensor (a_{ij}) is $a_{ij} = \frac{\overline{u'_i u'_j}}{k} - \frac{2}{3}\delta_{ij}$, and
ι is turbulence length scale ($\iota = k^{\frac{3}{2}}/\varepsilon$)

The viscous dissipation rate on the stress component is;

$$\varepsilon_{ij} = \nu \frac{\partial u'_i}{\partial x_j}\frac{\partial u'_j}{\partial x_i} \approx \frac{2}{3}\varepsilon\delta_{ij} \tag{8}$$

The viscous diffusion term is

$$d_{ijk} = d_{ijk}^{(p)} + d_{ijk}^{(u)} + \mu\frac{\partial \overline{u'_i u'_j}}{\partial x_k} = -\rho\overline{u'_i u'_j u'_k} - \overline{p' u'_j}\delta_{ik} - \overline{p' u'_i}\delta_{jk} + \mu\frac{\partial \overline{u'_i u'_j}}{\partial x_k} \tag{9}$$

Where $d_{ijk}^{(p)}$ is the viscous diffusion due to pressure and $d_{ijk}^{(u)}$ is the viscous diffusion due to velocity. In the accordance with a correlation of the generalized gradient diffusion hypothesis (GGDH) of Daly and Harlow [17], so Eq. (9) adapts to Eq. (10), in the form as

$$d_{ijk} = c_s\rho\frac{k}{\varepsilon}u'_k u'_l\frac{\partial \overline{u'_i u'_j}}{\partial x_l} + \mu\frac{\partial \overline{u'_i u'_j}}{\partial x_k} \tag{10}$$

Importantly, in order to accomplish the system equations, a turbulence dissipation rate (ε) equation or equivalent is also required. The implemented form is similar to those used in the standard k-ε schemes. The generalized form is Eq. (11).

$$\frac{\partial}{\partial t}(\rho\varepsilon) + \frac{\partial}{\partial x_i}(\rho\overline{U}_i\varepsilon) = \frac{\partial}{\partial x_i}\left[\left(\mu + \frac{\mu_t}{\sigma^{(\varepsilon)}}\right)\frac{\partial\varepsilon}{\partial x_i}\right] + \rho\left(C_{\varepsilon1}f_1P_k - C_{\varepsilon2}f_2\varepsilon\right)\frac{\varepsilon}{k} + \rho(S_l + S_\varepsilon) \tag{11}$$

where $P_k = \frac{1}{2}P_{ii}$ and all constants proposed in Launder et al. [18] in order to adjust the turbulence length scale and generation rate, also the standard wall function (WF) is advised to determine the turbulence in compliance with the law of wall, the assumption related to logarithmic near-wall velocity distribution along the normal distance of the wall, developed by the Manchester group [19].

3. NUMERICAL METHOD

This study applies 'OpenFOAM' version 7, which is under GNU General Public License [20]. The governing equations are discretized by finite volume scheme**.** In order to obtain the solution conforming to convergent criteria and low computational resource, the researcher decides the Gauss linear-upwind different scheme and the upwind different scheme to discretize a large number of turbulence and convection fluxes in the Tri-Diagonal Matrix Algorithm solver [21] with appropriate under-relaxation factor (0.2 and 0.4 for steady and unsteady case, respectively). Also, the Semi-Implicit Method for Pressure-Linked Equations (SIMPLE) is used to resolve the pressure from the velocity in the momentum equation.

3.1 Computational domain

These test cases have been carried out in the 3-dimensional analysis of Reynolds number of 10,000 70,026 and 96,000. The dimension and fluid properties have been converted from dimensionless groups using the scaling rule based on the components of Reynolds number. The example of the Reynolds number of 96,000 has been shown in Table 1.

Table 1: The grid density and turbulent flow properties of Reynolds number = 96,000.

Re = 96,000	**Number of Nodes**			**Turbulence fluxes**				**Momentum fluxes**	
kinematic viscosity (ν)	x (N_i)	y (N_j)	z (N_k)	intensity (I)	viscosity ratio (β)	kinetic energy (k)	dissipation rate (ε)	Inlet velocity vector	pressure
1.04167×10^{-5} m^2/s	100	100	100	1%	10	0.0001 m^2/s^2	8.64×10^{-6} m^2/s^3	(1,0,0) m/s	1 atm.

The structured mesh has been generated in the Cartesian coordinate system. The cube domain has been performed, which is 10 times of sphere diameter as shown in Fig. 1a. The near-wall meshes have been also refined, they have become inflation layers to obtain more smooth fluxes gradient along normal to the wall, moreover, the normal distance of the first layer located on the fully turbulent region on the standard wall function as Fig. 1b. Therefore, the non-dimensional distance (y^+) of near-wall nodes have been between 30-150. The boundary conditions have been identified for each face and wall, shown in Table 2, the constant pressure has been at the outlet flow. Apart from inlet and outlet faces, the flow has been periodic condition at couple faces. The turbulence level has been purposed by 1%, and also turbulent viscosity ratio has been identified as a factor of 10. Typically, the iteration method can be accomplished for a large number of unknown fluxes, they are solved in a diagonal matrix of finite volume scheme. Therefore, in the case of unsteady case, the incremental time (Δt) examines simply with second order interpolation of Crank-Nicolson scheme approximating as $\Delta t \leq \Delta x_j / U_\infty D$.

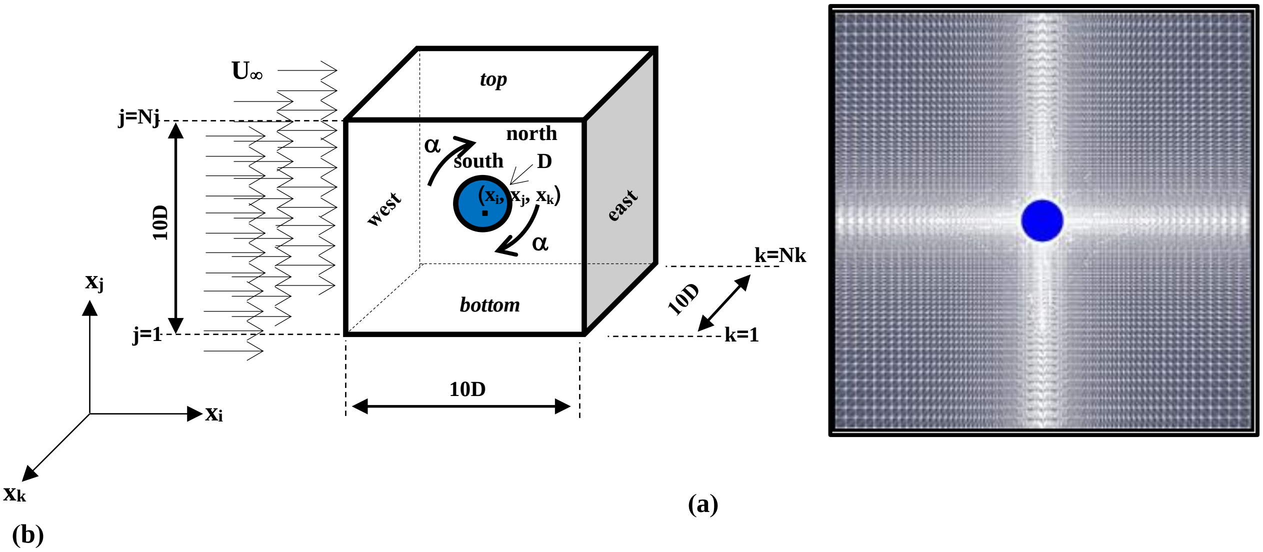

Fig. 1. Solution domain (a) 3D with face and (b) orthogonal grid.

Table 2: The boundary condition on cubic computational domain.

Face	Boundary Condition	U	V	W	k	ε	P
west	inlet	1	0	0	$(IU_\infty)^2$	$\frac{c_\mu k^2}{\beta \nu}$	$\frac{\partial P}{\partial x_i} = 0$
east	Far Field	$n \cdot \nabla U = 0$	$n \cdot \nabla V = 0$	$n \cdot \nabla W = 0$	$n \cdot \nabla k = 0$	$n \cdot \nabla \varepsilon = 0$	0
bottom	periodic I	$\phi_{j=1} = \phi_{j=Nj-1}$ and $\phi_{j=nj} = \phi_{j=2}$ when ϕ = U, V, W, k, ε and P					
top							
south	periodic II	$\phi_{k=1} = \phi_{k=Nk-1}$ and $\phi_{k=nk} = \phi_{k=2}$ when ϕ = U, V, W, k, ε and P					
north							
sphere	wall	$-\alpha U_\infty \sin\theta$	$\alpha U_\infty \cos\theta$	0	$\frac{\partial k}{\partial n} = 0$	$\frac{\partial \varepsilon}{\partial n} = 0$	$\frac{\partial P}{\partial n} = 0$

4. RESULTS AND DISCUSSION

4.1 Aerodynamic force coefficient time history

Figure 2 reports the dimensionless time history ($t^* = U_\infty t/D$) of lift (C_L) and drag (C_D) coefficients at Reynolds number of 96,000. These differences can be explained in the physical terms of unsteady RANS and RSM with standard wall function (WF). The RSM results in a stronger effect of frequency pattern and amplitude level for each period. Because the side force is a small effect on the sphere, inconsistent pattern have been found for all spin ratios. The computational result of the lift coefficient represents the RSM predicting the fluctuation data corresponding to the vortex alternate frequently shedding from shoulder sphere surfaces, whereas, the unsteady RANS shows a lower frequently alternating pattern for all spin ratios. Both models of turbulence present clearly, the spin ratios have a relevant effect on the magnitude level of lift coefficient, nevertheless, the predicted value is not greater than 0.7, these data are so small compared to a rotating cylinder test case [5]. The drag coefficient has also been calculated, which both models predicted similar patterns to the lift coefficient, but the amplitude is a little shorter than that range of lift coefficient. Those values of the drag coefficient have been less than 1, and the predicted data is a very close value between each of spin ratios up to 5. The predicted evidence has represented that the physical flow has been changing with instantaneous time, with can be calculated in time-average calculation data.

4.2 Time-Averaged aerodynamic coefficient

The competence of computational models has been evaluated in Table 3, which provided the validated prediction of lift and drag coefficients with earlier experimental studies. The drag coefficients are approximated to 0.50 and the present study can confirm a good closing value between those of them. It seems that the small discrepancy lift coefficient of those earlier experimental studies has been found, the earlier study provides the value of zero for symmetry flow and non-zero for a little asymmetry forming caused by a scale of time measurement. These results can confirm that both models have a performance carrying into execution of a rotating sphere.

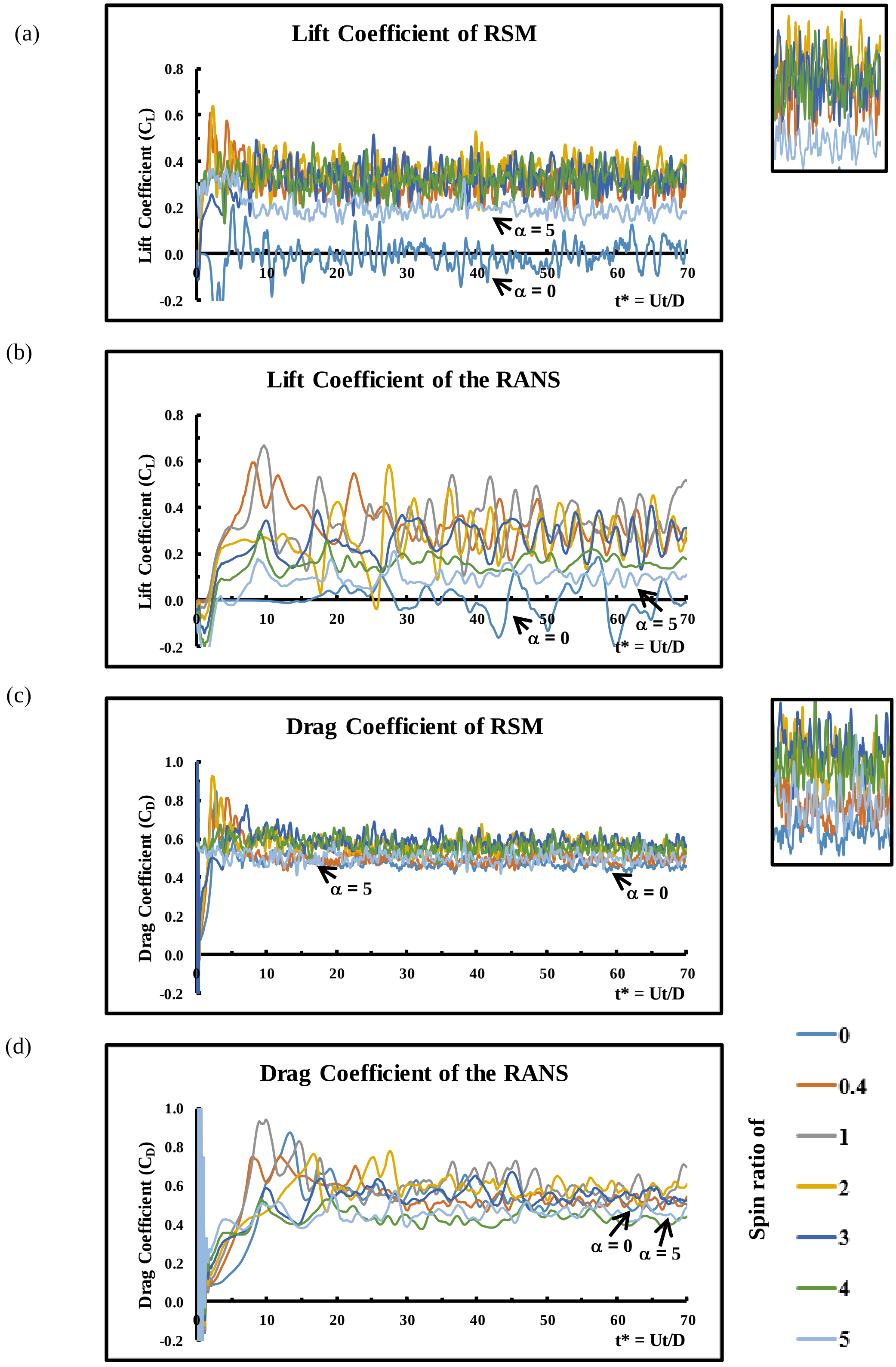

Fig. 2. The time history of aerodynamic coefficient of (a) lift coefficient predicted RSM (b) predicted RANS and (c) drag coefficient predicted RSM (d) predicted RANS at Reynolds number of 96,000.

Table 3: The aerodynamic coefficient of flow past a stationary sphere.

Flow Past a Stationary Sphere	Force Coefficient	
	Lift	**Drag**
Experimental Study : Achenbach [7] Re. = 96,000	No data	0.50
Experimental Study : Kray et al [9] Re. =96,000	0.01	0.52
Experimental Study : Kray et al [2] Re. =96,000	-0.03	0.50
Experimental Study : Kim et al [15] Re. =100,000	0.00	0.52
Experimental Study : Norman et al [3] Re. =110,000	0.07	No data
The Present Study Re. = 96,000		
The Reynolds Averaged Navier-Stoke Equation Model (Laminar approach, U-RANS)	0.00	0.49
The Reynolds Stress Equation with Standard Wall Function	-0.02	0.46

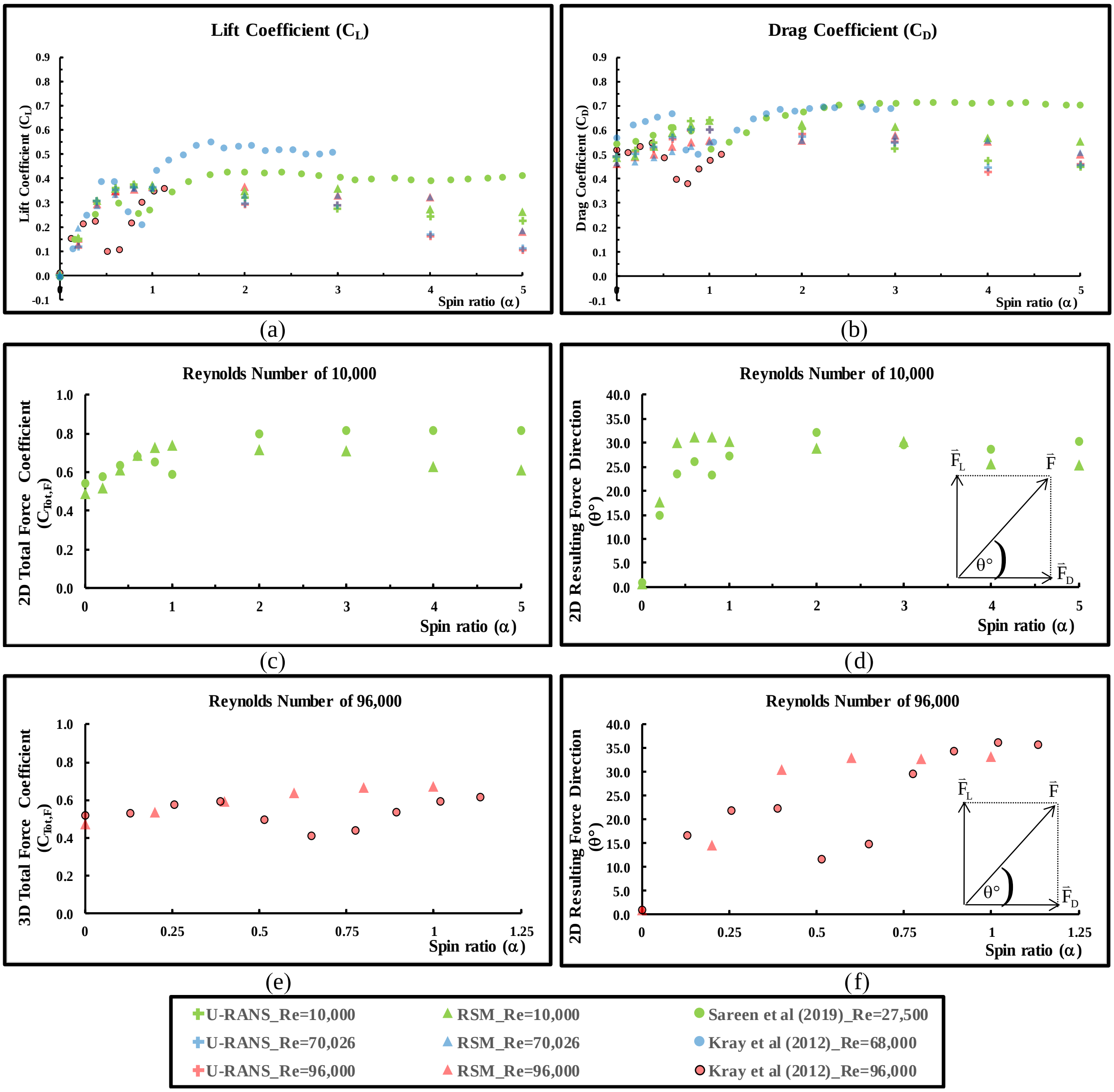

Fig. 3. The time-averaged aerodynamic coefficient of (a) lift (b) drag coefficient and (c) 2D total force and (d) resulting force direction at Re = 10,000 (e) 3D total force and (f) resulting force direction at Re = 96,000.

Figure 3 shows the comparison between prediction and measurement data of lift and drag coefficient over a range of spin ratios up to 5. The data have been provided in good agreement to examine the model's performance to predict the flow past a rotating sphere. In Fig. 3(a), as far as the lift coefficient is produced by a force perpendicular to the flow direction, their experimental studies [9, 22] report the data of spin ratio up to 1, 3 and 5 for Reynolds numbers of 96,000 68,000 and 27,500, respectively. The sudden drop of lift coefficients have appeared due to the laminar to turbulence transition along curvature surface, the present models are impossible to capture this characteristic for the range of small spin ratio between 0.4-0.8, the deviation results are similar to the LES prediction in a rotating cylinder of [5]. Apart from those spin ratios, the Reynolds stresses model (RSM) returns to predict a good agreement with those earlier experimental work. In the slow rotation speed up to 0.4, the lift coefficients continue increasing from the magnitude of zero to a higher value, then they suddenly drop and climb up again approaching the maximum C_L of 0.36 at spin ratio 1 for Reynolds number of 96,000. For extending the spin ratios greater than 1, the maximum C_L has been suggested depending on spin ratio and Reynolds number.

Figure 3(b) also presents the drag coefficient, the models has almost reached a constant value of 0.55 for spin ratios greater than 2. The Reynolds stresses model have been close to the measured value and the Reynolds averaged Navier-Stokes model (laminar approach) has been modest. The Reynolds stresses model predicts the increasing drag coefficient from 0.46 to 0.55 for spin ratios up to 1 at a high Reynolds number of 96,000. As spin ratios increased, the drag coefficient has a small change decreasing by 0.1. Also, the different Reynolds numbers provide insignificant different predicted data for each of the predicted approaches and spin ratios.

A small discrepancy in lift and drag coefficient has been obtained similar to previous predicted case of rotating cylinder, was reported by Karabelas et al. [23]. The total force coefficient has been measured to explain what the curious cause is in the under-prediction results, as Fig. 3(c) and 3(e). An entire spin ratio, the predicted total force coefficient ($C_{tot,F}$) has been very close to experimental data, especially the total force coefficient has been a little different of 0.9% when spin ratio becoming 0.4 and maximum difference has been found of 12% in case a spin ratio of 1 at Reynolds number of 96,000. Moreover, the small deviation result can be confirmed in the evidence of resulting force direction, which deviation angles have been 0.21°- 7.9° and 0.07°- 21° for Reynolds number of 10,000 and 96,000, respectively as shown in Fig. 3d and 3f. One interesting finding has been that resulting direction has been an association between the component force in lift and drag direction. In case of spin ratio between 0.5-0.8 at Reynolds number of 96,000, the unexpected result have been concerned due to laminar to turbulent boundary as mentioned in literature review.

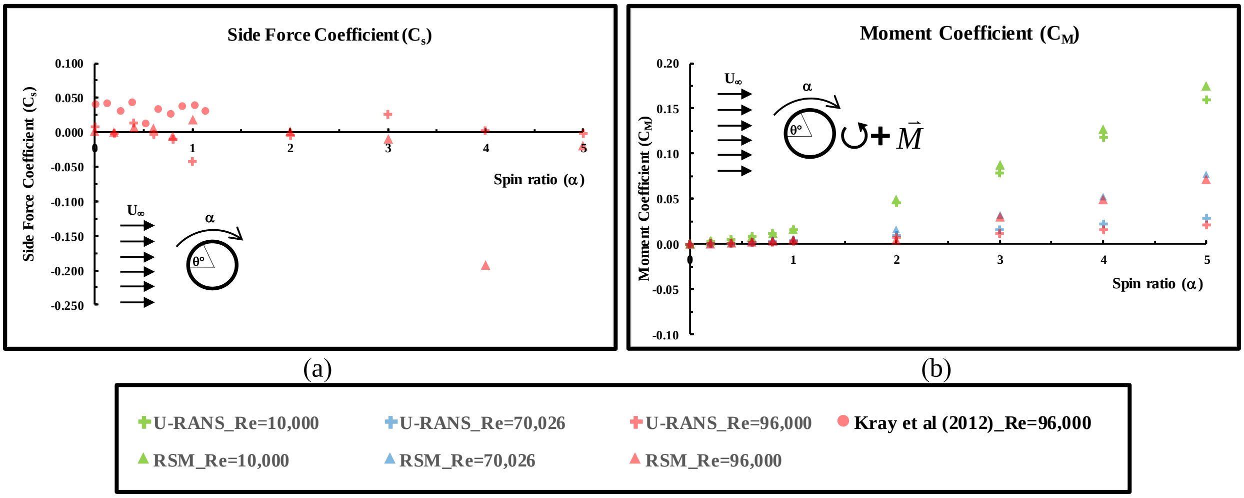

Fig. 4. A component aerodynamic in (a) side force coefficient and (b) moment coefficient predicted RSM.

Figure 4 also presents the side and moment coefficient performing on a rotating sphere. The side force randomly occurs in the z-direction. Figure 4(a) shows the side force coefficient (C_S) have been between (-0.042) - 0.0026 and (-0.19) - 0.018, predicted U-RANS and RSM respectively. The predicted C_s have been closing between each other for spin ratios apart of 4.

Moreover, Fig. 4 reports the moment coefficient driving on tangential curvature surface and opposed to rotating direction. Because the asymmetric flow has been captured, the resultant force has been the eccentricity of the sphere's centre. The pressure force cannot produce a moment because its direction past through the centre, but the viscous force is parallel to surface direction leading to produce the moment around the sphere leading to produce the body being fluctuated around yaw angle.

The predicted RSM provides a larger value of moment coefficient than U-RANS, it corresponds to the viscous force acting on the surface for each Reynolds number. In particular, the high viscous force has been found at low Reynolds numbers, consequently, the Reynolds number of 10,000 results in the largest moment coefficient over a range of the spin ratios. The alternated vortex shedding on the stationary sphere causes to produce a small moment coefficient of 8.5×10^{-6}, then it has greatly increased to 0.07 for a spin ratio of 5, predicted RSM at Reynolds number of 96,000. The moment coefficient tends in monotonically increasing and it can be suggested that the graph has been fitted in the quadratic polynomial with the spin ratio as $0.003\alpha^2 - 0.0005\alpha + 0.0007$.

4.3 Pressure contribution

The pressure distributions of a rotating sphere have been measured in pressure coefficient. Figure 5 shows an asymmetric pattern around parallel to flow direction (azimuthally angle of 180°). The pressures have been strongly fluctuating along the circumference, and they have been obviously uncertainly between closing azimuthally angles because the flows have interacted between each 3D plane for spin ratios greater than 2. The stagnation position has located at maximum pressure. The graphs have presented the stagnation positions of 0°, -1.43° and -1.43° for spin ratios up to 2, respectively. Therefore, the stagnation flow has translated along the circumference in the opposite rotating direction. Whereas, the suction flows have been found at the azimuthally angle of the lowest pressure. The suction pressures on acceleration side move along circumference in the same rotating direction, they have been found at azimuthally angles of 72.44°, 88.57° and 88.57° when increasing spin ratios up to 2. Therefore, the tangential velocity of the rotating sphere can superimpose the dynamic flow energy, when the flow has not been enough energy to overcome the shear force on the surface, consequently, the flow becomes a separating behavior.

Figure 6 has also presented the component forces, including pressure and viscous terms. The result show the pressure, has dominated on total force for a range of spin ratios. The RSM predicts the closing pressure value with U-RANS for spin ratios less than 3. RSM results in the minimum and maximum pressure coefficient of 0.47 and 0.66, for a stationary and spin ratio of 1, whereas, U-RANS predicts those values of 0.45 and 0.69, for spin ratios of 4 and 0.8, respectively. Those approaches provide much less viscous coefficient than pressure coefficient and they have tended to increase monotonically for spin ratios growing up. It is important that the viscous forces are less than 2% of pressure forces for spin ratios less than 3, so the viscous force can be neglected, however, it can be approximated by 7% for a spin ratio of 5, predicted RSM approach.

Figure 7 has also presented the Q-Criterion iso-surface and velocity field on the computational domain. The Q-criterion has been defined as $\mathrm{Q} = \frac{1}{2}[\Omega^2 - \mathrm{S}^2]$ and indicated the separating rate between the flow layers. The volume scale has been captured at the range of 5. A high thickness has been given on both sphere shoulders for the stationary case. As the sphere becomes rotating, the flow thickness has remained on the deceleration side coloring by high turbulent kinetic energy. The right hand side of Fig. 7 shows the velocity field, which represents the wake behind a stationary sphere and an almost symmetric pattern. When the sphere becomes rotating (spin ratio of 5), the vortex shedding has expanded far away from the surface.

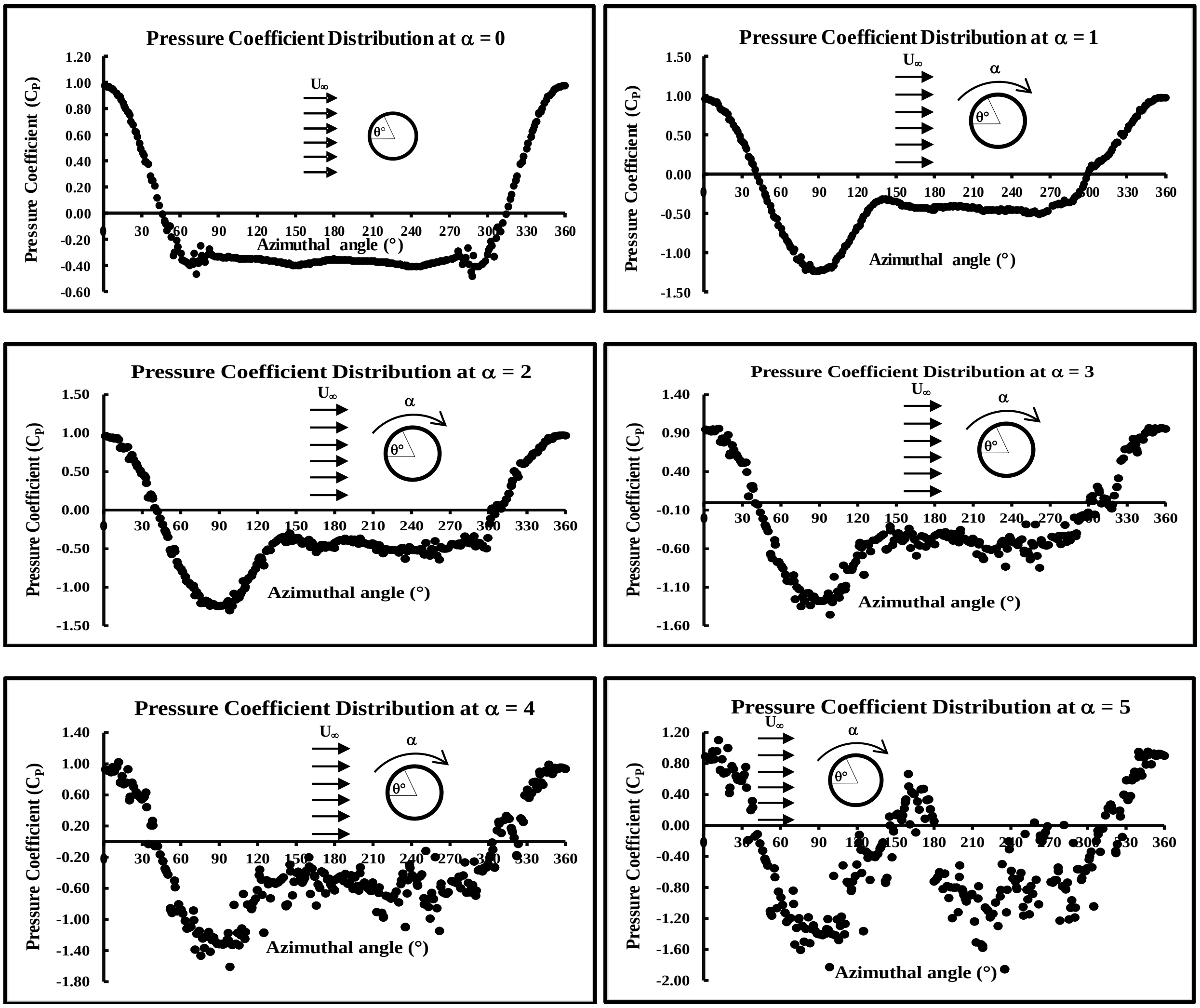

Fig. 5. The pressure contribution around a stationary and rotating sphere predicted RSM at Reynolds number of 96,000.

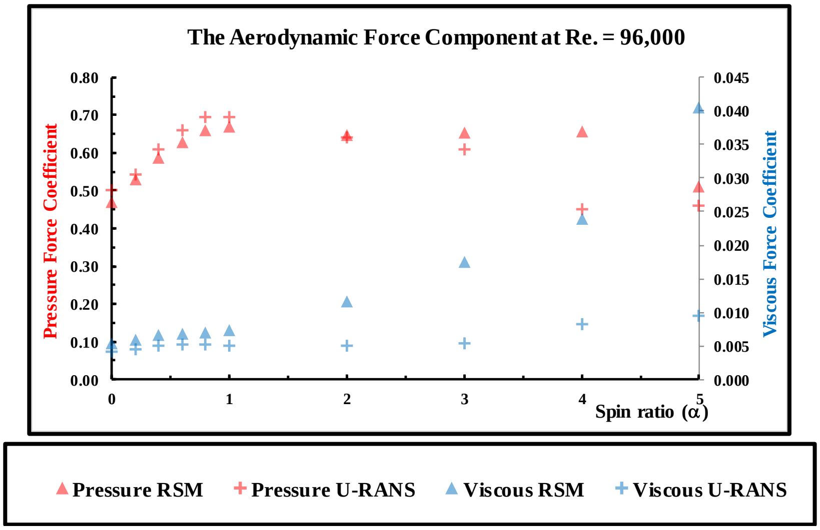

Fig. 6. The aerodynamic force component including pressure and viscous force at Re. = 96,000.

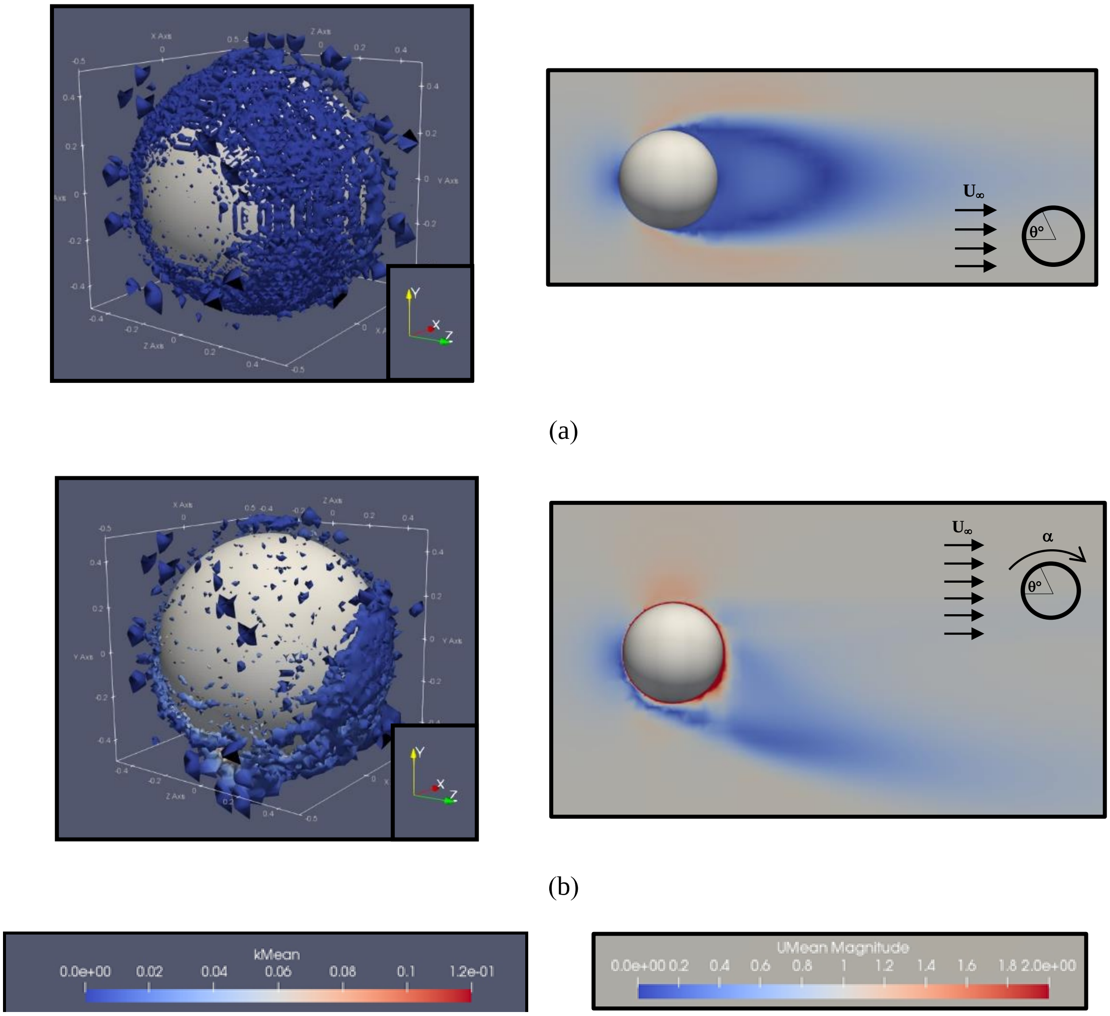

(a)

(b)

Fig. 7. The time-averaged k contour on Q-Criterion iso-surface of 5 (left) velocity field (right) for spin ratio of (a) zero and (b) 5 predicted RSM at Reynolds number of 96,000.

5. CONCLUSION

The RSM approach with a standard near wall function has competence enough to investigate the convective flow past a rotating sphere at high Reynolds number. The evidence of k contour is to suggest that the turbulent fluxes have to be considered in the flow domain because the flow has interacted with the curvature surface of the sphere, the flow are fully turbulent phenomena and it has been strongly 3-dimensional effect leading to obtain uncertainly vortex shedding frequency pattern with increasing time. As the sphere become rotating up to 1, the lift coefficient increase to a maximum value of 0.36, then they have been a small decrease for those spin ratios greater than 1, whilst the drag coefficient has been higher than lift coefficient, it has been around 0.55. Whereas the side force coefficient have been little scale, they have been around (-0.19) - 0.018 for a range of spin ratio, predicted RSM approach. The largest magnitude of the aerodynamic force is generated due to the pressure, it has corresponded to the critical points of wall boundary layer such as suction and stagnation position, they have also translated along the circumference in the same or opposite to rotating sphere directions. Moreover, the pressure distributions have been asymmetry around parallel to flow direction leading to produce aerodynamic force as increasing spin ratio. The moment has been also produced by the viscous force in tangential direction of circumference and it has been monotonically increased with the opposite to rotating direction for spin ratio up to 5.

ABBREVIATIONS/NOMENCLATURE

a_{ij}	anisotropic stress tensor
C_D	drag coefficient
C_L	lift coefficient
C_s	side force coefficient
$C_{tot,F}$	total force coefficient
$C_{\varepsilon 1}$, $C_{\varepsilon 2}$	constant of ε eq. (1.44, 1.92)
c_s	diffusion process coefficient (0.22)
c_{1w}, c_{2w}	constant for RSMs (0.5, 0.3)
c_μ	eddy diffusivity coefficient (0.09)
c_1, c_2	constant for RSMs (1.8, 0.6)
D	diameter
d_{ijk}	viscous diffusion
f_1, f_2	closure coefficient of ε eq. (1, 1)
f_μ	damping factor
I	turbulent intensity
i,j,k,l,m	matrix or stress tensor
k	turbulent kinetic energy
n	normal unit vector
P, p'	mean and fluctuation pressure
P_k	turbulence generation rate
	Prandl number (1.3)
Q	criterion iso-surface
RANS	Reynolds averaged Navier-Strokes
Re	Reynolds number
RSM	Reynolds stress model
S	mean strain tensor
S_l, S_ε	length scale and ε source term
t, t*	time, dimensionless time
U,u'	mean and fluctuation velocity
U-RANS	unsteady Reynolds averaged Navier-Strokes (Laminar approach)
U_∞	free stream velocity
x_i, x_j, x_k	coordinate of 1st,2nd, 3rd axis
y, y^+	non / dimensionless wall distance
α	spin ratio
β	viscosity ratio
δ_{ij}	Kronecter delta 1(i=j) or 0 (i≠j)
ε	turbulent dissipation rate
θ	azimuthal angle
μ,ν	kinetic and dynamic viscosity
ρ	density
$\sigma^{(k)}$	turbulent Prandl number (1.0)
$\sigma^{(\varepsilon)}$	turbulent diffusivity
Φ_{ij}	pressure-strain correlation
Ω	mean ration tensor
ω	angular velocity
$\overline{\ }$	average
t	turbulence subscript
w	wall superscript

ACKNOWLEDGEMENT

This research was supported by the institute for research and development, Sukhothai Thammathirat Open University (Grant no. FPS 9/2562). The author would like to thank the OpenFOAM Foundation for the free software under GNU General Public License. Also, the developed turbulent approach and computing technique from Thermo-Fluids Research Group of the University of Manchester, UK have been valuable to accomplish this high turbulence on strongly curvature surface work.

REFERENCES

[1] Magnus, G. Ueber die Abweichung der Geschosse, und: Ueber eine auffallende Erscheinung bei rotirenden Körpern, Annalen der Physik, Vol. 164(1), 1853, pp. 1-29.

[2] Kray, T., Franke, J. and Frank, W. Magnus effect on a rotating soccer ball at high Reynolds numbers, Journal of Wind Engineering and Industrial Aerodynamics, Vol. 124, 2014, pp. 46-53.

[3] Norman, A.K., Kerrigan, E.C. and McKeon, B.J. The effect of small-amplitude time-dependent changes to the surface morphology of a sphere, Journal of Fluid Mechanics, Vol. 675, 2011, pp. 268-296.

[4] Pijush, K.K. and Ira, M.C. Fluid Mechanics, 3rd edition, 2004, Academic Press, Cambridge.

[5] Aoki, K. and Ito, T. Flow characteristics around a rotating cylinder, paper presented in Proceedings of the School of Engineering of Tokai University, 2001, Tokai University, Japan.

[6] Johnson, T.A. and Patel, V.C. Flow past a sphere up to a Reynolds number of 300, Journal of Fluid Mechanics, Vol. 378, 1999, pp. 19-70.

[7] Achenbach, E. Experiments on the flow past spheres at very high Reynolds numbers, Journal of Fluid Mechanics, Vol. 54, 1972, pp. 565-575.

[8] Wieselsberger, C. Neuere Feststellungen uber die Gesetze des Flussigkeits und Luftwiderstands, Physikalische Zeitschrift, Vol. 22, 1921, pp. 321-328.

[9] Kray, T., Franke, J. and Frank, W. Magnus effect on a rotating sphere at high Reynolds numbers, Journal of Wind Engineering and Industrial Aerodynamics, Vol. 110, 2012, pp. 1-9.

[10] Li, Z. and Gao, N. Experimental study of flow around a rotating sphere at a moderate Reynolds number, paper presented in the ASME 2018 5th Joint US-European Fluids Engineering Division Summer Meeting, 2018, Montreal, Canada.

[11] Dobson, J., Ooi, A. and Poon, E.K.W. The flow structures of a transversely rotating sphere at high rotation rates, Computers and Fluids, Vol. 102, 2014, pp. 170-181.

[12] Lee, S. A numerical study of the unsteady wake behind a sphere in a uniform flow at moderate Reynolds numbers, Computers and Fluids, Vol. 29(6), 2000, pp. 639-667.

[13] Sadikin, A., Mohd Yunus, N.A., Abdullah, K. and Mohammed, A.N. Numerical study of flow past a solid sphere at moderate Reynolds number, Applied Mechanics and Materials, Vol. 660, 2014, pp. 674-678.

[14] Kim, D. and Choi, H. Large eddy simulation of turbulent flow over a sphere using an immersed boundary method, paper presented in the Third AFOSR International Conference on DNS/LES, 2001, University of Texas at Arlington, United States.

[15] Constantinescu, G.S. and Squires, K.D. LES and DES Investigations of turbulent flow over a sphere at Re = 10,000, Flow, Turbulence and Combustion, Vol. 70, 2003, pp. 267-298.

[16] Poon, E.K.W., Iaccarino, G., Ooi, A.S.H. and Giacobello, M. Numerical studies of high Reynolds number flow past a stationary and rotating sphere, paper presented in Proceedings of the 7th International Conference on CFD in the Minerals and Process Industries, 2009, Melbourne, Australia.

[17] Daly, B.J. and Harlow, F.H. Transport equation in turbulence, Physics of Fluids, Vol. 13, 1970, pp. 2634-2649.

[18] Launder, B.E., Reece, G.J. and Rodi, W. Progress in the development of a Reynolds-stress turbulence closure, Journal of Fluid Mechanics, Vol. 68, 1975, pp. 537-566.

[19] Craft, T.J., Gerasimov, A.V., Iacovides, H. and Launder, B.E. Progress in the generalization of wall-function treatments, International Journal of Heat and Fluid Flow, Vol. 23(2), 2002, pp. 148-160.

[20] The OpenFOAM Foundation. OpenFOAM 7.0, London, United Kingdom, URL: https://openfoam.org/, accessed on 02/12/2021, 2019.

[21] Thomas, L.H. Elliptic problems in linear differential equations over a network, 1949, Columbia University, New York.

[22] Sareen, A., Zhao, J., Lo Jacono, D., Sheridan, J., Hourigan, K. and Thompson, M. Flow past a transversely rotating sphere, paper presented in 11th International Conference on Flow-Induced Vibrations, 2016, The Hague, Netherlands.

[23] Karabelas, S.J., Koumroglou, B.C., Argyropoulos, C.D. and Markatos, N.C. High Reynolds number turbulent flow past a rotating cylinder, Applied Mathematical Modelling, Vol. 36(1), 2012, pp. 379-398.